Multifunctional human serum albumin-crosslinked and self-assembling nanoparticles for therapy of periodontitis by anti-oxidation, anti-inflammation and osteogenesis

Bangping Cao [a], Xuanbo Da [b], Wenjing Wu [a], Jian Xie [a], Xuejing Li [a], Xin Wang [a], Hui Xu [a], Jianfang Gao [a], Hui Yang [a], Jiansheng Su [a,*]

[a] Shanghai Engineering Research Center of Tooth Restoration and Regeneration & Tongji Research Institute of Stomatology & Department of Prosthodontics, Stomatological Hospital and Dental School, Tongji University, Shanghai, China
[b] Department of General Surgery, Second Affiliated Hospital of Xi'an Jiaotong University, Xi'an, Shaanxi, 710000, China

ARTICLE INFO

ABSTRACT

Periodontitis is a chronic inflammatory disease that can result in the irreversible loss of tooth-supporting tissues and elevate the likelihood and intensity of systemic diseases. The presence of reactive oxygen species (ROS) and associated related oxidative stress is intricately linked to the progression and severity of periodontal inflammation. Targeted removal of local ROS may serve to attenuate inflammation, improve the unfavorable periodontal microenvironment and potentially reverse ensuing pathological cascades. These ROS scavenging nanoparticles, which possess additional characteristics such as anti-inflammation and osteogenic differentiation, are highly sought after for the treatment of periodontitis. In this study, negative charged human serum albumin-crosslinked manganese-doped self-assembling Prussian blue nanoparticles (HSA-MDSPB NPs) were fabricated. These nanoparticles demonstrate the ability to scavenge multiple ROS including superoxide anion, free hydroxyl radicals, singlet oxygen and hydrogen peroxide. Additionally, HSA-MDSPB NPs exhibit the capacity to alleviate inflammation in gingiva and alveolar bone both *in vitro* and *in vivo*. Furthermore, HSA-MDSPB NPs have been shown to play a role in promoting the polarization of macrophages from the M1 to M2 phenotype, resulting in reduced production of pro-inflammatory cytokines. More attractively, HSA-MDSPB NPs have been demonstrated to enhance cellular osteogenic differentiation. These properties of HSA-MDSPB NPs contribute to decreased inflammation, extracellular matrix degradation and bone loss in periodontal tissue. In conclusion, the multifunctional nature of HSA-MDSPB NPs provides a promising therapeutic approach for the treatment of periodontitis.

1. Introduction

Periodontitis, a chronic inflammatory disease of periodontal tissue, is distinguished by the degradation of the periodontal ligament and loss of peripheral alveolar bone. This condition is a significant public health concern globally, impacting more than 60 % of dentate adults [1]. Furthermore, periodontitis is recognized as a primary contributor to the loss of masticatory function and is associated with an increased risk of various systemic diseases, including cardiovascular disease, diabetes, rheumatoid arthritis, Alzheimer's disease, cancer and so forth [2–7]. Given the well-documented adverse effects associated with antibiotics, anti-inflammatory agents [8,9] and the singularity of their function, as

well as the unpleasant side effects of mechanical debridement and surgery [10], there is a growing need for a non-surgical, multi-functional, and safe alternative for managing periodontitis.

The presence of excessive ROS in inflamed periodontal tissues not only leads to oxidative stress and cellular damage, but also triggers the production and release of inflammatory cytokines and hydrolases [11, 12]. Meanwhile, ROS play a role in the process of osteoclast formation as an intracellular signaling molecule [13], leading to the loss of periodontal attachment and alveolar bone. Thus, the effective clearance of ROS in the periodontal microenvironment is crucial for protecting cells and tissues from damage and is a key aspect of periodontitis therapy.

Nanoparticles possessing ROS scavenging capabilities through

---

multiple catalytic activities offer distinct advantages over natural enzymes, such as cost-effectiveness, enhanced stability, diverse and superior catalytic activities, increased design flexibility, and additional functionalities beyond catalysis [14,15]. Examples of such functional nanoparticles include cerium dioxide, trimanganese tetraoxide, Prussian blue (PB), and others, which find applications in various fields including colitis, ischemic stroke, neurodegenerative diseases, pancreatitis,

rheumatoid arthritis, among others [14,16,17]. PB nanoparticles exhibit enzyme-like catalytic properties as a result of the presence of both Fe^{3+} and Fe^{2+} ions [18,19]. The incorporation of additional transition metals into PB has the potential to enhance its enzyme-like activities and introduce novel functionalities. Manganese, a ubiquitous transition metal, plays a crucial role in the structure of various biological antioxidant enzymes, including catalase, mitochondrial superoxide dismutase,
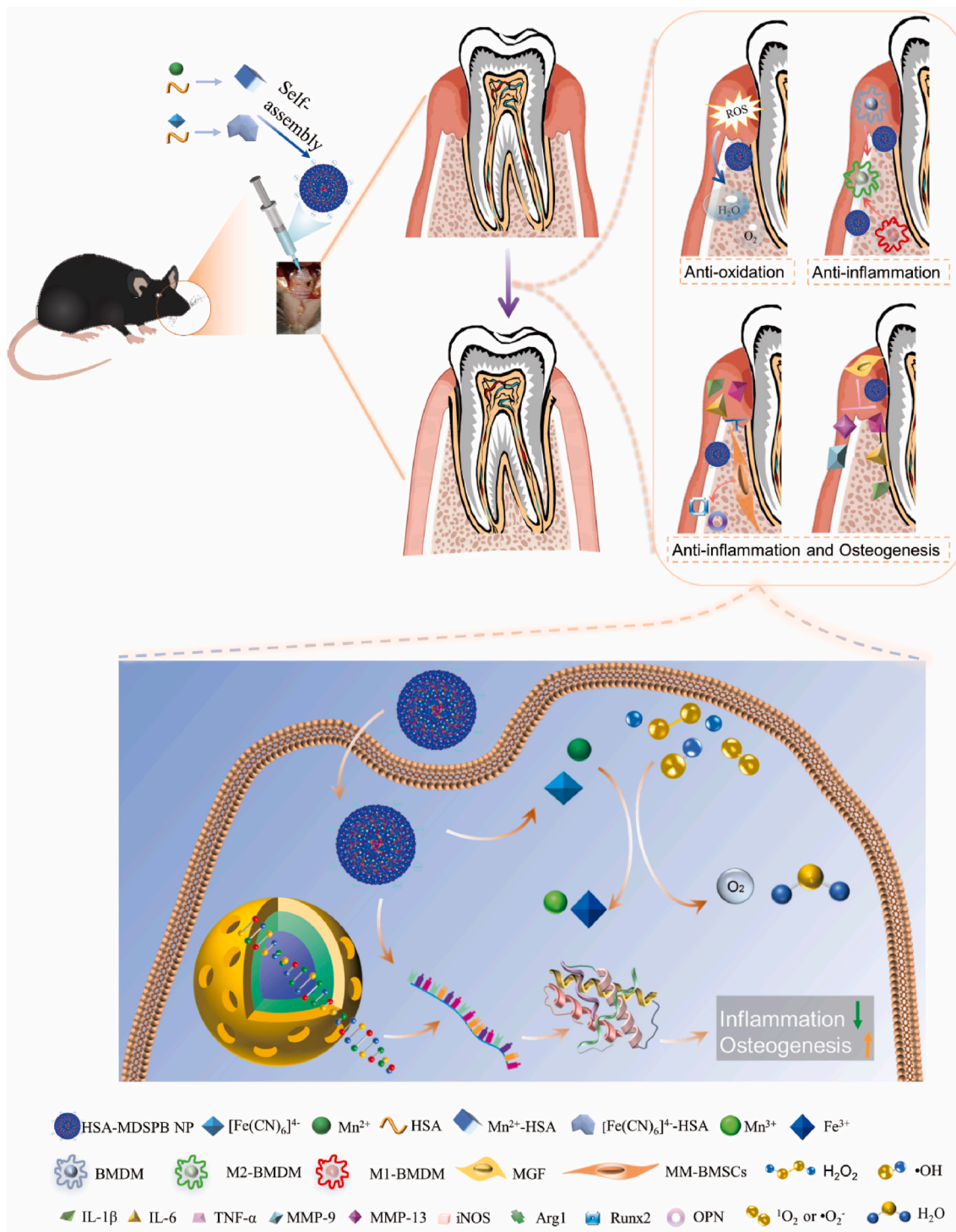

Scheme 1. A schematic illustration detailing the synthesis of HSA-MDSPB NPs and their application in periodontitis therapy is provided. The negatively charged HSA-MDSPB NPs were synthesized through the self-assembly process involving HSA, $[Fe(CN)_6]^{4-}$ and Mn^{2+}. HSA-MDSPB NPs exhibit the ability to scavenge multiple ROS in periodontal cells and tissues by virtue of their enzyme-like activities, possess anti-inflammatory properties, promote the transformation of BMDM cell type, and induce the expression of osteogenic genes. These characteristics make HSA-MDSPB NPs a promising candidate for the treatment of periodontitis.

and peroxidase [20], and has been shown to impact osteogenic differentiation [21–24]. Serum albumin, a naturally occurring protein, possesses N-terminal amine and cysteine residues with high coordination affinity towards transition metal ions including Au^{3+}, Cu^{2+}, Gd^{3+} and Bi^{3+}, among others. This protein is anticipated to adopt a conformation resembling an expanding hollow nanocage due to its abundance of charged groups and molecular chains flexibility [25–27]. Human serum albumin (HSA), as an endogenous protein, has been approved by the Food and Drug Administration for intravenous administration [28] and is extensively investigated in the field of anti-tumor drug delivery systems to enhance targeting efficacy and reduce adverse effects, among other potential applications [27,29,30]. However, the efficacy of HSA in crosslinking transition metals manganese (Mn) and iron (Fe) to produce modified PB nanoparticles with enhanced antioxidant, anti-inflammatory, and osteogenic properties, as well as their potential therapeutic impact on periodontitis, remains uncertain.

This study successfully synthesized HSA-crosslinked manganese-doped self-assembling Prussian blue nanoparticles, composed of HSA,

Mn^{2+} and $[Fe(CN)_6]^{4-}$, for the treatment of periodontitis (Scheme 1). HSA exhibited low biotoxicity and immunogenicity, along with superior physiological properties, making it suitable for chemical modifications and drug delivery. Additionally, Mn^{2+} and Fe^{2+} contributed to ROS scavenging, anti-inflammatory and osteogenic effects. The negative charge of HSA-MDSPB NPs may facilitate their accumulation and adhesion to positively charged inflamed periodontal tissues. Furthermore, the HSA-MDSPB NPs demonstrated the ability to mitigate periodontal inflammation and bone resorption through their various capacities for scavenging reactive oxygen species, anti-inflammatory effects, immune regulation, and promotion of osteogenesis in both *in vitro* and *in vivo* studies. In summary, the presented HSA-MDSPB NPs exhibit promising therapeutic potential for the treatment of periodontitis, and potentially other diseases with similar pathophysiological mechanisms.
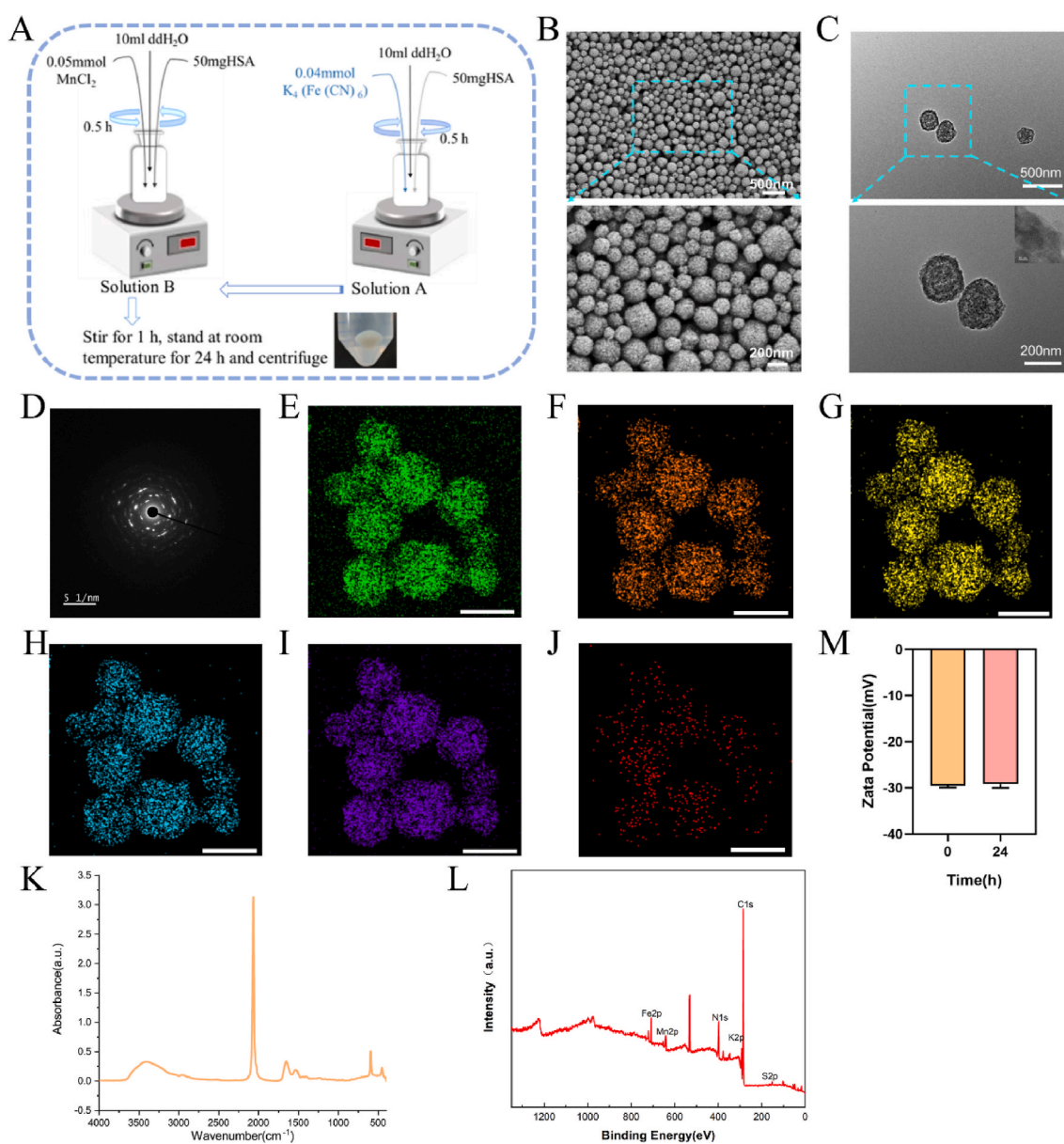
Fig. 1. Synthesis and characterization of HSA-MDSPB NPs. (**A**) The process diagram of synthesis of HSA-MDSPB NPs. (**B**) SEM images of HSA-MDSPB NPs. (**C**) TEM images of HSA-MDSPB NPs. (**D**) High-resolution TEM image of HSA-MDSPB NPs. (**E-J**) The element mapping (C, Fe, K, Mn, N and S) of HSA-MDSPB NPs (scale bar = 250 nm). (**K**) FTIR Spectrometer of HSA-MDSPB NPs. (**L**) XPS spectral of HSA-MDSPB NPs. (**M**) Zeta potentials of HSA-MDSPB NPs.

2. Results and discussion

2.1. Synthesis and characterization of HSA-MDSPB NPs

The role of HSA in enhancing the properties of the nano-materials is highlighted [14,31]. The synthesis of HSA-MDSPB NPs is depicted in Fig. 1A. HSA serves as a natural protein nanoreactor, functioning as chelators for Mn^{2+} and $[Fe(CN)_6]^{4-}$ and a pore-making agent. The morphology of Mn^{2+}-HSA and $[Fe(CN)_6]^{4-}$-HSA was observed directly through scanning electron microscopy (SEM) (Figs. S1A and B), while SEM and transmission electron microscope (TEM) images were used to visualize the morphology of HSA-MDSPB NPs (Fig. 1B and C), showcasing a high degree of crystallinity (Fig. 1D) that positions them as a potential drug delivery system. These nanoparticles also demonstrated good physical dispersion and size stability, with a diameter of approximately 250 nm (Figs. S2A–C). The chemical composition of HSA-MDSPB NPs was further confirmed through energy-dispersive X-ray spectroscopy. The successful synthesis of HSA-MDSPB NPs was confirmed through the analysis of Fig. 1E–J, which demonstrated the presence and uniform distribution of C, Fe, K, Mn, N, S. Furthermore, the chemical structures of HSA-MDSPB NPs were detected through Fourier transform infrared (FTIR) spectroscopic analysis and X-ray photoelectron spectroscopy (XPS). The presence of -OH and –CO–NH peaks in the HSA-MDSPB NPs indicated the incorporation of HSA, further supporting the successful synthesis of HSA-MDSPB NPs (Fig. 1K). XPS analyses further revealed the chemical composition of the HSA-MDSPB NPs with wide scan spectrum confirming the presence of Fe, Mn, C, N, K and S (Fig. 1L). According to the data presented in Fig. 1M, the zeta potential analysis indicated that the HSA-MDSPB NPs possessed a negative charge, which remained consistent after a 24-h period. This negative charge is believed to facilitate the accumulation of the nanoparticles at inflammatory location with a positive charge, due to the strong electrostatic attraction between oppositely charged materials [32].
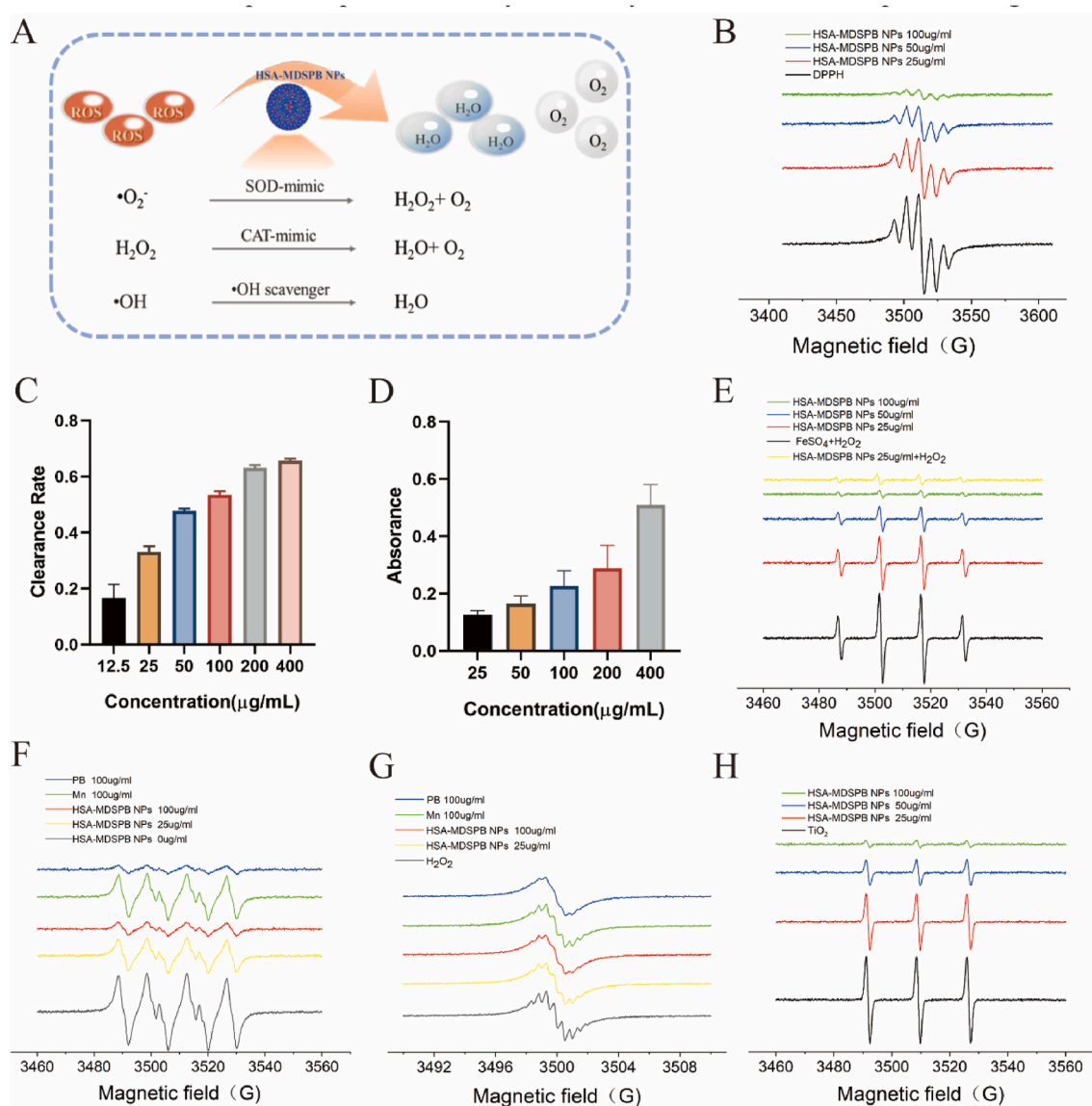
Fig. 2. ROS scavenging capabilities of HSA-MDSPB NPs. (**A**) A schematic illustration of the antioxidative capabilities of HAS-MDSPB NPs. (**B–C**) The total antioxidant capacity of HSA-MDSPB NPs by DPPH and ABTS assays. (**D**) The POD enzyme activity of HSA-MDSPB NPs. (**E**) The •OH eliminating efficiency of HSA-MDSPB NPs by EPR. (**F**) The superoxide anion scavenging ability of HSA-MDSPB NPs by EPR. (**G**) The H_2O_2 scavenging ability of HSA-MDSPB NPs by EPR. (**H**) Singlet oxygen eliminating ability of HSA-MDSPB NPs by EPR.

2.2. ROS scavenging capacities of HSA-MDSPB NPs

Reactive oxygen species (ROS), comprising various unstable molecules including hydrogen peroxide (H_2O_2), hydroxyl radicals (•OH), superoxide anion (•O_2^-), singlet oxygen ($^1O_2$) and so forth, are produced as byproducts of physiological metabolism and are typically neutralized by the antioxidant defense system under normal conditions [33,34]. Excessive levels of ROS in periodontitis tissue contribute to the progression of the disease [35,36]. The transition metal ion nanoparticle HSA-MDSPB NPs, as presented in Fig. 2A, demonstrate the ability to scavenge not only •O_2^- and H_2O_2 because of their superoxide dismutase and catalase-like activities, but also •OH. Prior to assessing the ROS scavenging capabilities of HSA-MDSPB NPs, the release kinetics of Mn^{2+} and $[Fe(CN)_6]^{4-}$ from the HSA-MDSPB NPs were investigated. It was demonstrated that a gradual release of Mn^{2+} and $[Fe(CN)_6]^{4-}$ occurred within the initial 72-h period, with higher levels of release observed in the pH 6.5 group (Fig. S3A). Furthermore, Mn^{2+} exhibited a higher release rate compared to $[Fe(CN)_6]^{4-}$. Then to confirm the ROS scavenging capabilities of HSA-MDSPB NPs, an indirect verification method was employed, wherein the absorbance of 1,1-diphenyl-2-trinitrophenyl-hydrazine (DPPH) was monitored as an indicator of ROS radicals following interaction with HSA-MDSPB NPs. Electron paramagnetic resonance (EPR) spectra demonstrated a decrease in absorbance value with increasing concentrations of HSA-MDSPB NPs (Fig. 2B). The total ROS scavenging capacity of HSA-MDSPB NPs was determined using the [2,2′-Azinobis-bis(3-ethylbenzthiazoline-6-sulphonate)] (ABTS) assay, where the ABTS radical cation's absorption peak was observed at 734 nm. The presence of antioxidants led to a decrease in absorbance value. Analysis of Fig. 2C indicated that HSA-MDSPB NPs at a concentration of 200 μg/mL exhibited a total free radical scavenging capacity exceeding 60 %, suggesting a robust antioxidant capability. The concentration-dependent peroxidase enzyme activity was confirmed, as depicted in Fig. 2D.

EPR spectroscopy was further utilized to investigate the scavenging capabilities of HSA-MDSPB NPs. The generation of •OH through the reaction of $FeSO_4$ and H_2O_2 was employed to assess the efficacy of HSA-MDSPB NPs in eliminating free radicals. The results confirmed the ability of HSA-MDSPB NPs to neutralize free radicals, with the efficiency of elimination showing a concentration-dependent relationship (Fig. 2E). The SOD-like activity of HSA-MDSPB NPs was confirmed through their introduction into a superoxide anion generating system comprising xanthine and xanthine oxidase (Fig. 2F). Furthermore, the capacity of HSA-MDSPB NPs to scavenge H_2O_2 was evidenced by EPR analysis and the observation of bubble formation upon their introduction into an H_2O_2 solution (Fig. 2G and Fig. S3B). Importantly, this scavenging ability was demonstrated in the absence of the Fenton reaction (Fig. 2E, first line), which typically leads to the generation of harmful free radicals that can induce cellular damage. $^1O_2$ is identified as a distinct type of ROS characterized by its potent oxidizing properties. The scavenging of $^1O_2$ by HSA-MDSPB NPs was confirmed through EPR using 2,2,6,6-tetramethyl-4-piperidinone hydrochloride as a capture agent, while TiO_2 was utilized for the generation of singlet oxygen under ultrasound irradiation conditions. Consistent with expectations, the EPR signal exhibited a gradual decline with increasing concentration of HSA-MDSPB NPs (Fig. 2H). Collectively, these findings highlight the exceptional scavenging efficacy of HSA-MDSPB NPs towards various ROS.

2.3. Biocompatibility and antioxidant property in vitro

The premise for the permissible use of biomaterials lies in their advantageous biocompatibility. To assess the biosafety of HSA-MDSPB NPs, we conducted *in vitro* evaluations using mouse gingival fibroblasts (MGF), a crucial component of periodontal soft tissue, and mouse maxillary bone marrow stromal cells (MM-BMSCs), which play a vital role in periodontal hard tissue, through cell counting kit-8 (CCK-8) assay. The results indicate that the viability of MGF and MM-BMSCs cells

cultured with HSA-MDSPB NPs at different concentrations exceeded 90 %, with some even surpassing 100 %, suggesting that HSA-MDSPB NPs at these concentrations exhibit favorable biosafety (Figs. S4A and S5A). Consequently, we employed HSA-MDSPB NPs at these concentrations for subsequent experiments.

The accumulation of ROS contributes to increased oxidative stress within cells and tissues, ultimately giving rise to the worsening of periodontal inflammation and alveolar bone resorption [37]. Due to the observed ROS scavenging abilities of HSA-MDSPB NPs and their uptake by cells through endocytosis as confirmed by fluorescence microscopy and flow cytometry (Fig. S6A-B, S7A-B, S8A-B and S9A-B), we further investigated the cellular antioxidant properties of HSA-MDSPB NPs. Following the confirmation of *Escherichia coli* lipopolysaccharide (LPS)-induced cellular oxidative stress, the antioxidant activity of the HSA-MDSPB NPs was evaluated using a ROS probe 2,7-dichlorodihydrofluorescein diacetate (DCFH-DA). As depicted in Fig. 3A and B, Fig. S4B, S5B-C, the LPS group exhibited a significant increase in ROS generation compared to the CON group, as evidenced by a stronger fluorescence signal. Conversely, treatment with HSA-MDSPB NPs resulted in a reduction in ROS level, indicating a mitigating effect on endogenous oxidative stress. In summary, HSA-MDSPB NPs demonstrated cellular antioxidant properties.

2.4. Cellular anti-inflammatory and osteogenic properties

To investigate the anti-inflammatory properties of HSA-MDSPB NPs, an LPS-induced inflammatory condition was triumphantly established using MGF, MM-BMSCs, and bone marrow derived macrophages (BMDM), which partake in the innate immune response to periodontal pathogen infection during the initiation and resolution of inflammation [38,39], followed by detection of inflammatory and immunoregulatory factors. Results presented in Fig. 3C–G and Figs. S10A–C demonstrate that LPS stimulation led to increased secretion of interleukin-1β and −6 (IL-1β and −6), tumor necrosis factor-α (TNF-α), matrix metalloproteinase-9 and -13 (MMP-9 and -13) in MGF, while the expression of these factors were significantly suppressed in LPS + HSA-MDSPB group. In addition, the levels of IL-6 and TNF-α were evaluated via enzyme-linked immunosorbent assay (ELISA) (Fig. 3H and I), and the results were in line with those obtained from Western blot (Fig. 3L), showing that HSA-MDSPB NPs could counteract the inflammation response triggered by LPS. As revealed in Figs. S11A–E, the mRNA and protein expression levels of IL-1β, IL-6 and TNF-α were upregulated by LPS and downregulated by the HSA-MDSPB NPs, confirming the potent anti-inflammatory effects of the HSA-MDSPB NPs on MM-BMSCs. Throughout the entire process of the innate immune defense, macrophages show remarkable flexibility and can be activated in a dualistic manner, ultimately bringing about the secretion of miscellaneous cell factors to fight against stimuli [40,41]. iNOS and Arg1 serve as classical biomarkers for the M1 phenotype, which releases pro-inflammatory cytokines including TNF-α, and the M2 phenotype, which releases anti-inflammatory cytokines including interleukin-10 (IL-10), respectively [42–44]. To validate the cellular immunoregulatory capabilities, similar assessments were also conducted using BMDM. As anticipated, the results uncovered that compared to the CON and LPS + HSA-MDSPB groups, the expression of iNOS was noticeably increased in the LPS group (Fig. 3J, M). Conversely, the Arg1 protein was up-regulated in the LPS + HSA-MDSPB groups in contrast with LPS group (Fig. 3M). Besides, the expression of IL-1β, IL-6 and TNF-α was the most with the least of IL-10 in the LPS group, whereas treatment with HSA-MDSPB NPs significantly decreased the secretion of IL-1β, IL-6 and TNF-α accompanied by increased IL-10 in comparison to LPS group (Fig. S12A-F and Fig. 3K). These results provide evidence that HSA-MDSPB NPs possessed inspiring characteristics in terms of oxidation and inflammation resistance.

Considering the significance of bone generation in the reversal of periodontal defects, the evaluation of the osteogenic property of HSA-
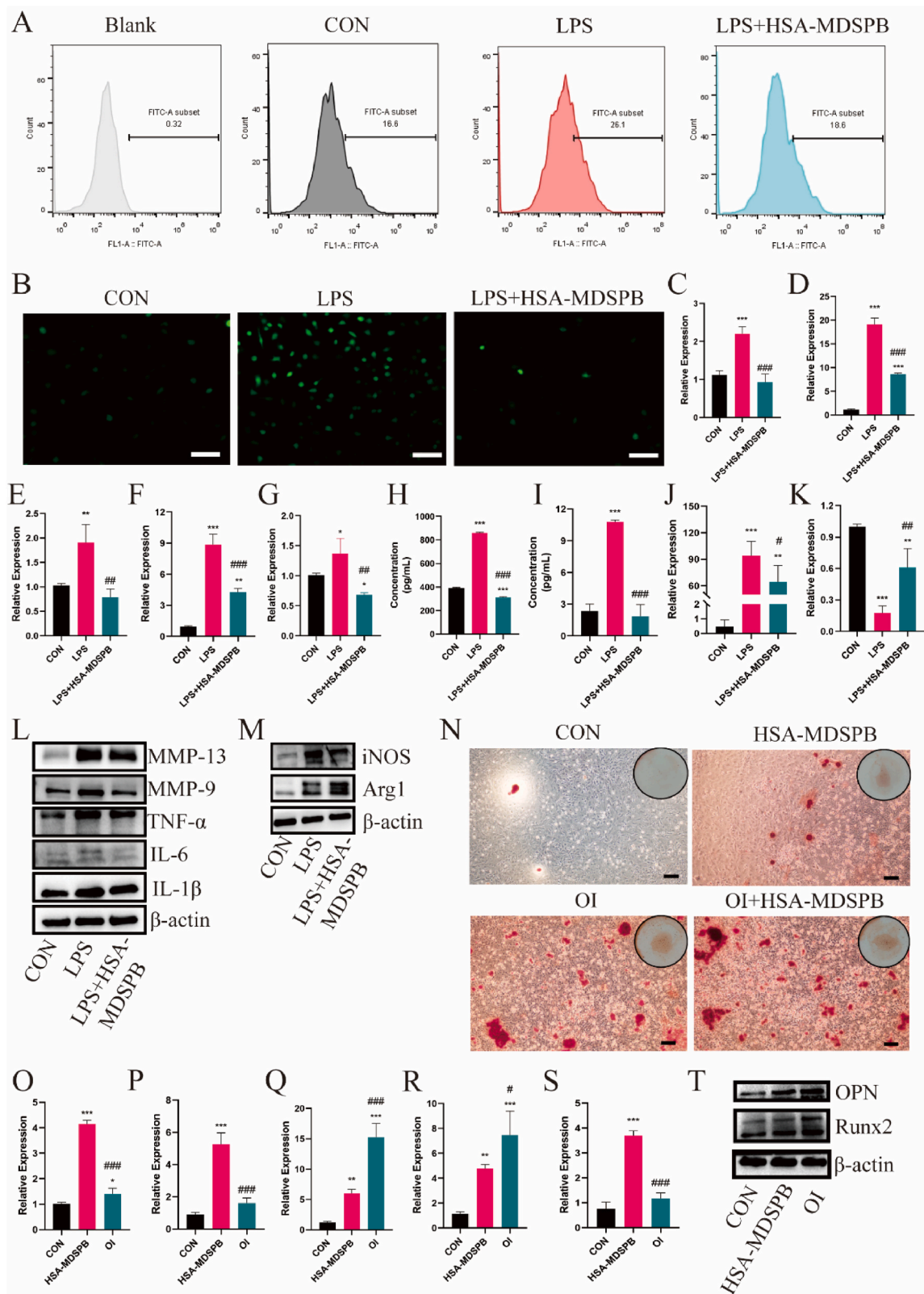
Fig. 3. Cellular antioxidation, anti-inflammatory and osteogenic properties of HSA-MDSPB NPs *in vitro*. (**A**) The fluorescence intensity (DCFH-DA) of MGF with different treatments. (**B**) Representative fluorescence images of BMDM with different treatments stained by DCFH-DA (Green) (scale bar = 100 μm). (**C-G**) Analysis of the relative expression of IL-1β, IL-6, TNF-α, MMP-9, and MMP-13 mRNA in MGF treated with different treatments. (**H, I**) Quantification of the concentrations of IL-6 and TNF-α in the culture medium supernatant of MGF with different treatments. (**J, K**) Evaluation of the relative expression levels of iNOS and IL-10 mRNA in BMDM with different treatments. Western blot analysis of MGF (**L**) and BMDM (**M**) with different treatments. (**N**) ARS staining of MM-BMSCs (21 days) with different treatments (scale bar = 100 μm). (**O–S**) Assessment of the relative expression of Runx2, OCN, OPN, BSP, and DMP1 mRNA in MM-BMSCs with different treatments (7 days). (**T**) Western blot analysis of MM-BMSCs with different treatments (7 days). n = 3, */#$p < 0.05$, **/##$p < 0.01$, ***/###$p < 0.001$, * VS CON, # VS LPS/HSA-MDSPB.

MDSPB NPs was conducted through alizarin red S (ARS), quantitative real-time polymerase chain reaction (qRT-PCR) assay, and western blot analysis. ARS is a well-established method for validating mineralized nodules [45]. As shown in Fig. 3N and Fig. S13A, the mineralized nodules in HSA-MDSPB group and osteogenic induction (OI) + HSA-MDSPB group were larger and more abundant than those of CON group and OI group respectively at 14 and 21 days, indicating the ability of HSA-MDSPB NPs to promote cell mineralization. Moreover, the expressions of osteogenic genes such as Runt-related transcription factor 2 (Runx2), osteopontin (OPN), bone sialoprotein (BSP), osteocalcin (OCN) and dentin matrix protein 1 (DMP1) [46–49], and their corresponding proteins including Runx2 and OPN were up-regulated by HSA-MDSPB NPs while the gene expression levels of OPN and BSP in OI group exceeded those in HSA-MDSPB group (Fig. 3O–T, Figs. S14A–E), which means HSA-MDSPB NPs might facilitate osteogenic differentiation to a slightly different degree compared to conventional osteogenic induction mixtures, potentially due in part to the presence of Mn (Figs.S15A-K). Therefore, it was reasonable to conclude that HSA-MDSPB NPs possess osteogenic capabilities.

2.5. In vivo antioxidant and anti-inflammatory property

Prior to evaluating the antioxidant capability of HSA-MDSPB NPs *in vivo*, their retention in periodontal tissue and distribution in various organs such as the heart, liver, spleen, lung and kidneys was confirmed using an *in vivo* imaging system (Figs. S16A and B). The results indicated that the HSA-MDSPB NPs remained in the tissues for a minimum of 48 h post-injection and were likely metabolized primarily by the liver and kidney. Then ROS levels were monitored by a living imaging system after the treatments illustrated by Fig. 4A and Fig. S17A. According to the results presented in Fig. 4B and C, a notable increase in fluorescence signals was observed in the LPS group in comparison to the CON group, while the Ligature-induced periodontitis (LIP) + HSA-MDSPB group showed much lower fluorescence signals, which were similar to those observed in groups receiving different treatments over a 14-day period (Figs. S17B and C). All above revealed the satisfactory removal of ROS by HSA-MDSPB NPs *in vivo*. Furthermore, to assess the anti-inflammatory properties of HSA-MDSPB NPs *in vivo*, levels of inflammatory cytokines IL-1β, IL-6, TNF-α, MMP-9, MMP-13 and myeloperoxidase (MPO) in the periodontium was measured. As depicted in Fig. 4D–G and Figs. S18A–F, the mRNA expression levels of IL-1β and −6, TNF-α, MMP-9, -13 and −8 in gingiva tissue exhibited a significant downward trend when comparing the LIP + HSA-MDSPB groups to the corresponding LIP groups. Similarly, the mRNA expression of IL-1β and −6 as well as TNF-α in maxillary bone was much less in the LIP + HSA-MDSPB groups compared to the LIP groups, regardless of whether they had been treated for 7 or 14 days (Fig. 4H–J, Figure S19A-C). At the same time, immunofluorescence images uncovered fluorescence intensity of MPO, IL-1β and MMP-9 was increased in the LIP group by contrast with the CON group, while treatment with HSA-MDSPB NPs could normalize these elevated fluorescence signals (Fig. 4K, L, M). These findings confirmed that the application of HSA-MDSPB NPs could effectively eliminate surplus ROS *in vivo* and improve the inflammatory microenvironment associated with periodontitis.

2.6. Comprehensive effect of HSA-MDSPB NPs in ligature-induced periodontitis

To further investigate the efficacy of HSA-MDSPB NPs in preventing loss of periodontal tissue, a classical ligature-induced periodontitis model [50] was established as showed in Fig. S20A, and HSA-MDSPB NPs were administered to the periodontium. Subsequent micro-computed tomography (Micro-CT) imaging and histological staining were proceeded to appraise the therapeutic outcomes at 7 and 14 days post-surgery. The vertical distance between the alveolar bone crest (ABC) and the cementoenamel junction (CEJ) of the second molar in

micro-CT 3D reconstructed images was considered as a therapeutic indicator. Meanwhile, quantitative analysis of bone volume/tissue volume (BV/TV) and bone mineral density (BMD) was processed through micro-CT. The results displayed that the distance between the buccal or lingual ABC and the corresponding CEJ in LIP group was much greater than that of CON group, whereas the same distance in LIP + HSA-MDSPB group was significantly reduced compared to the LIP group (Fig. 5A–C, Figs. S21A–C). Furthermore, the use of silk ligature gave rise to a significant decrease in bone parameter values (BV/TV and BMD) in comparison to CON group, a decrease that was reversed by the utilization of HSA-MDSPB NPs (Fig. 5D–E, Figs. S21D–E). All of these revealed the striking reduction in alveolar bone caused by ligature-induced periodontitis, and the effectiveness of HSA-MDSPB NPs in mitigating bone loss and promoting osteogenesis. Hematoxylin and eosin (H&E) staining of the periodontal tissue certified substantial periodontal attachment loss in the LIP group, with less attachment loss observed in the LIP + HSA-MDSPB group (Fig. 5F and Fig. S22A). Collagen, a structural component in bone, contributes to the tensile strength of natural bone [51]. Obvious collagen (Blue) degeneration, inflammatory cell infiltration and bone loss were revealed in LIP group by Masson staining, while these abnormalities were ameliorated in the LIP + HSA-MDSPB group (Fig. 5G). In conclusion, HSA-MDSPB NPs could effectively alleviate the destruction of the periodontal tissue by mitigating inflammation and promoting tissue regeneration.

2.7. Biosafety of HSA-MDSPB NPs in vivo

To examine the *in vivo* biosafety of HSA-MDSPB NPs, tail vein injections were administered at concentrations of 10 mg/kg and 20 mg/kg. After a three-week period, H&E staining was performed on spleen, heart, lung, liver, and kidney obtained from each experimental group, and no notable inflammation or pathological changes were found in any of the examined organs (Fig. S23A), similar to those in organs from mice that received injections every other day for 7 and 14 days (Fig. S24A). Additionally, serum was collected to assess liver and kidney function. No obvious difference was discovered in liver function markers, including alanine aminotransferase (ALT) and aspartate aminotransferase (AST) among the groups (Figs. S23B and C). Urea (UREA) and creatinine (CREA), the representative of kidney function parameters, were found to be within normal range (Figs. S23D and E). Finally, a blood routine test was conducted, revealing no significant changes in any of the indexes when any two groups were compared (Figs. S23F–N). All these results manifested the encouraging biosafety of HSA-MDSPB NPs *in vivo*.

2.8. Gene expression analysis

To reveal the potential mechanisms underlying the anti-inflammatory and antioxidant character of HSA-MDSPB NPs, gene expression in MM-BMSCs was firstly measured through RNA-seq in the LPS + HSA-MDSPB group compared to the LPS group. By analyzing, 999 genes expression were enhanced while 1119 genes were suppressed in the LPS + HSA-MDSPB group. The distribution of these DEGs was visualized on volcano plots (Fig. 6A). A compilation of the top 30 changed genes engaged in immune defense is presented in Fig. 6B. Compared to the LPS groups, plenty of differentially expressed genes were uncovered in the LPS + HSA-MDSPB group and were found to be enriched in inflammation-related pathways, such as HIF-1, NF-kappa B, MAPK, IL-17 and chemokine signaling pathways as determined through KEGG pathway enrichment analysis (Fig. 6C). In addition, a Gene Ontology (GO) analysis was also carried out, and remarkable difference was discovered between the two groups in hypoxia-inducible factor-1 alpha signing pathway, macrophage activation involved in immune response and MAP kinase phosphatase activity, as well as MHC class I protein complex and so forth (Fig. 6D). All of them might play a certain role in the inflammatory response. Interestingly, differential expressing genes were also found in vascular endothelial growth factor production
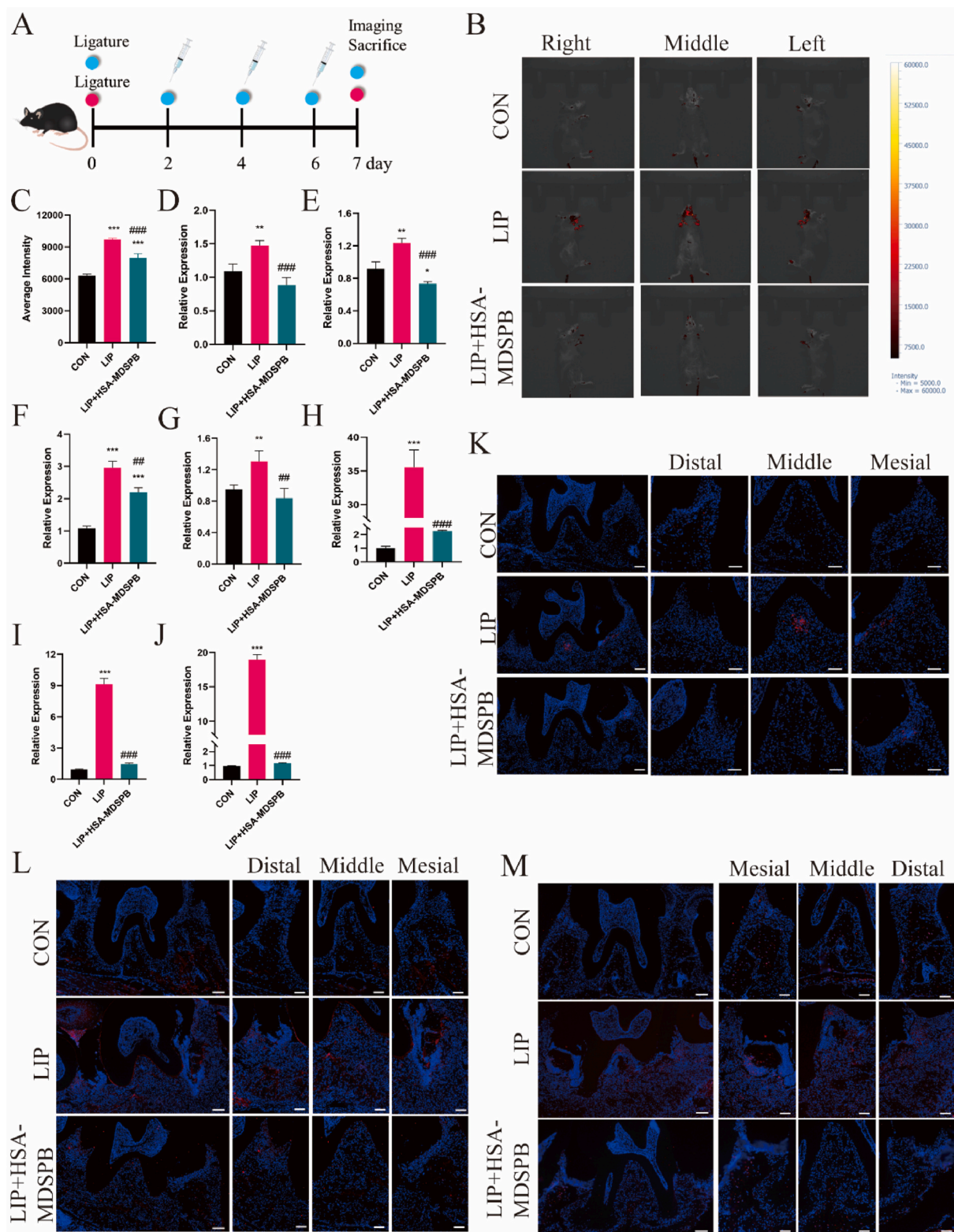
Fig. 4. *In vivo* antioxidant and anti-inflammatory properties of HSA-MDSPB NPs. (**A**) A schematic representation of the Ligature-induced periodontitis model (Red circle) and the HSA-MDSPB-treatment LIP model (blue circle). (**B–C**) Live imaging of small animals and quantitative analysis of ROS stained by L012 in periodontal tissue with different treatments (7d). (**D-G**) The relative expression of IL-6, TNF-α, MMP-9, and MMP-13 mRNA in the gingiva with different treatments (7d). (**H-J**) The relative expression of IL-1β, IL-6, and TNF-α mRNA in the maxillary bone with different treatments (7d). Immunofluorescent staining for MPO(**K**), IL-1β(**L**) and MMP-9 (**M**) in the periodontal tissue (Blue-nuclei, red-MPO/IL-1β/MMP-9) (scale bar = 100 μm). n = 3, *$p < 0.05$, **/##$p < 0.01$, ***/###$p < 0.001$, * VS CON, # VS LIP.
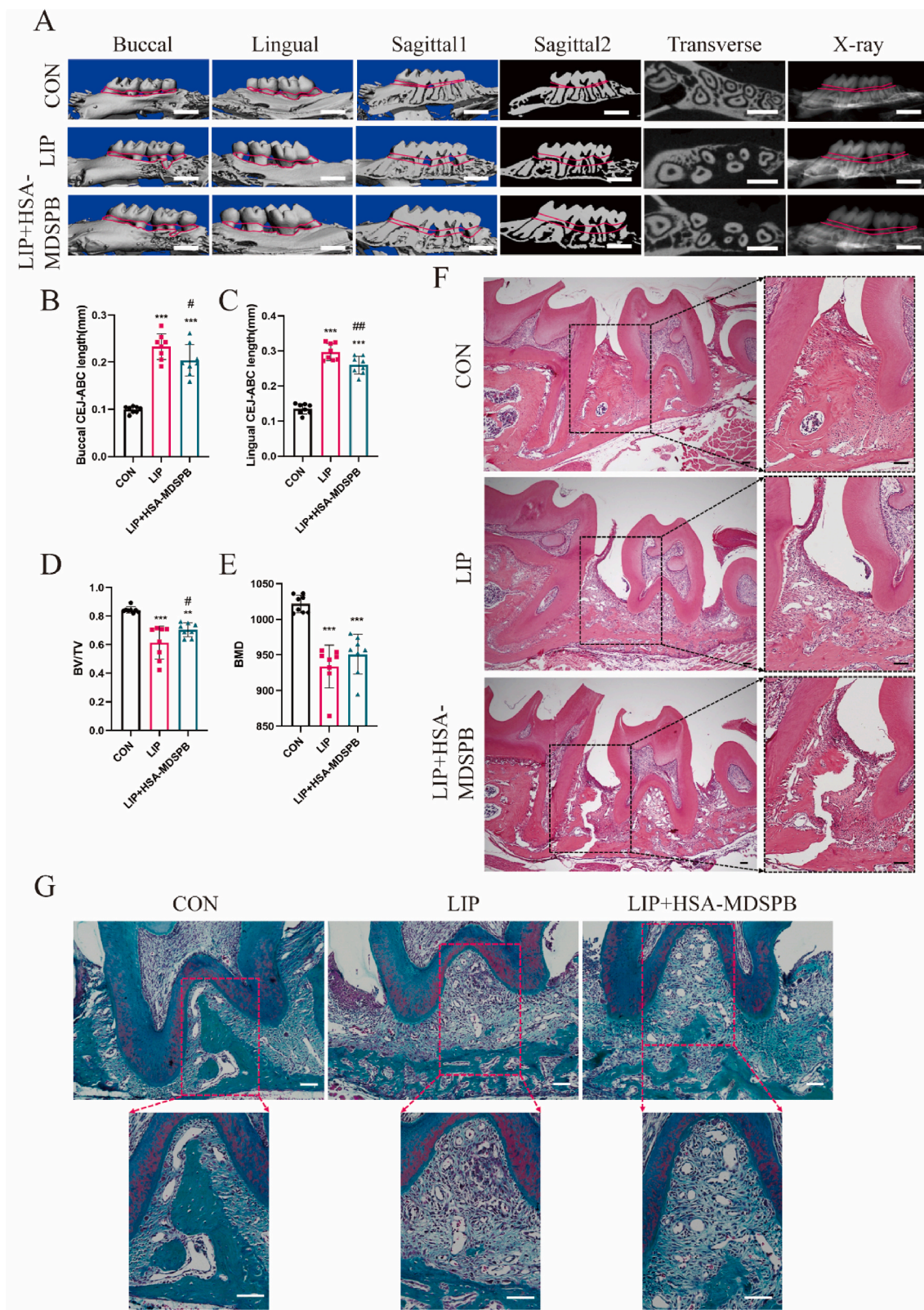
Fig. 5. Comprehensive therapeutic effect of HSA-MDSPB NPs in periodontitis. (**A**) 3D reconstructed images of the maxillary molars with different treatments (7 days) by Micro-CT. Red lines represent the distance between the ABC and the CEJ (scale bar = 1 mm). (**B, C**) Quantitative evaluations of the distance between the ABC and the CEJ from the buccal and lingual sides of the second molar. (**D, E**) The quantitative statistics on different parameters of the alveolar bone. (**F**) H&E staining images of the periodontal tissue (scale bar = 100 μm). (**G**) Masson staining images of the periodontal tissue (scale bar = 100 μm). n ≥ 3, #p < 0.05, **/##p < 0.01, ***p < 0.001, * VS CON, # VS LIP.
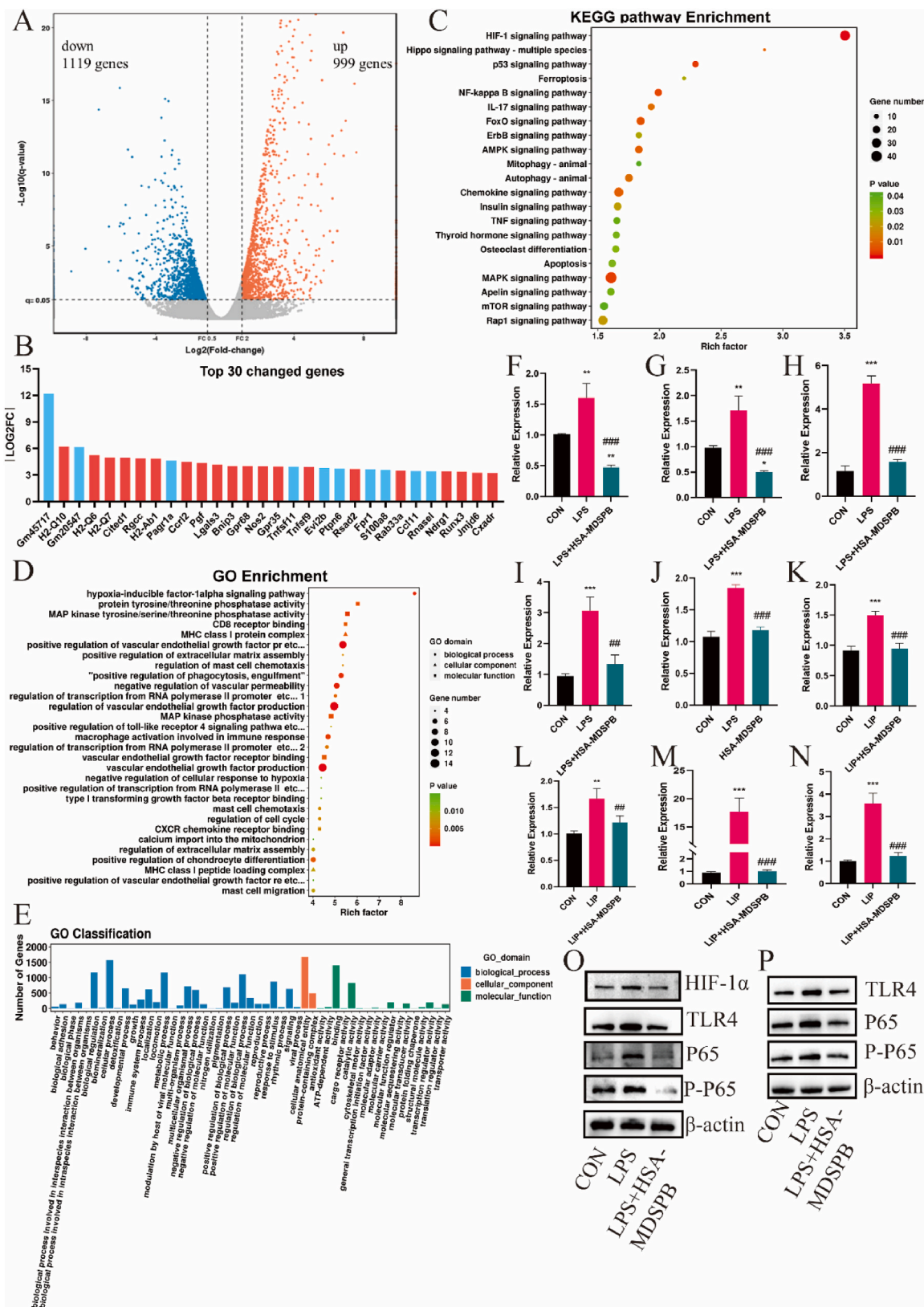
Fig. 6. RNA-seq assessments of MM-BMSCs treated with HSA-MDSPB NPs. (**A**) A volcano plot illustrating significant gene expression changes in the (LPS + HSA-MDSPB)/LPS comparison. (**B**) Genes related to the immune system process identified through GO classification analysis and the top 30 changed genes. (**C**) KEGG pathway enrichment analysis of differential genes. (**D**) GO classification analysis of differential genes. (**E**) Quantification of gene expression involved in BP, CC and MF was quantified. (**F, G**) The relative expression of TLR4 and P65 mRNA in MGF with different treatments. (**H-J**) The relative expression of TLR4, P65, and HIF-1α mRNA in MM-BMSCs with different treatments. (**K, L**) The relative expression of TLR4 and P65 mRNA in the gingiva with different treatments (7d). (**M, N**) The relative expression of TLR4 and P65 mRNA in the maxillary bone with different treatments (7d). (**O**) Western blot analysis of MM-BMSCs with different treatments. (**P**) Western blot analysis of BMDM with different treatments. n = 3, *$p < 0.05$, **/##$p < 0.01$, ***/###$p < 0.001$, * VS CON, # VS LPS/LIP.

and positive regulation of chondrocyte differentiation between the LPS + HSA-MDSPB group and the LPS group, which means HSA-MDSPB NPs may contribute to the process of angiogenesis and chondrogenesis (Fig. 6D). This phenomenon is believed to be associated with the presence of manganese [52–54] or other materials such as PB [55–58], warranting further exploration. As illustrated in Fig. 6E, more genes in the LPS + HSA-MDSPB group were found to be related to molecular functions, cellular components, and biological processes than in the LPS group. Then, we demonstrated the toll-like receptor-NF-kappa B pathway and HIF-1α might be involved in the anti-inflammation effects of HSA-MDSPB NPs further by assaying toll-like receptor 4 (TLR4), P65, and HIF-1α mRNA and protein expression, as well as P–P65 protein expression. The results showed the participation of HSA-MDSPB NPs made the mRNA expression of TLR4 and P65 in the LPS + HSA-MDSPB group decreased significantly compared to the LPS group in both MGF and MM-BMSCs (Fig. 6F–I), consistent with observations in gingiva and maxillary bone (Fig. 6K–N). Additionally, the TLR4, P65 and P–P65 protein of MM-BMSCs and BMDM co-cultured with HSA-MDSPB NPs expressed at lower levels in comparison to the LPS group (Fig. 6O and P). Finally, HIF-1α mRNA and protein expression were suppressed by HSA-MDSPB NPs compared to the LPS group (Fig. 6J and O).

To elucidate the potential mechanisms underlying the osteogenic properties of HSA-MDSPB NPs, gene expression in MM-BMSCs was assessed via RNA-seq in the HSA-MDSPB group relative to the CON group. Through analysis, it was observed that 735 genes exhibited decreased expression while 789 genes showed upregulation in the HSA-MDSPB group. The distribution of these DEGs was visually represented on volcano plots (Fig. S25A), revealing associations with various molecular functions, cellular components, and biological processes (Fig. S25B). Additionally, differential gene expression analysis was conducted on the HSA-MDSPB group compared to the CON group by KEGG pathway enrichment analysis, which revealed distinct patterns in genes associated with the PI3K-AKT, Wnt, and MAPK signaling pathways known to play a role in osteogenesis [59–61], as illustrated in Fig. S25C. Moreover, a GO analysis was performed, revealing discrepancies between the two groups in the regulation of bone resorption, positive regulation of osteoblast differentiation, bone mineralization, and the regulation of the BMP signaling pathway, which has been linked to osteogenesis [62], among other factors (Fig. S25D).

In general, these findings illustrated that HSA-MDSPB NPs may function as a promising treatment for periodontitis. Our data was beneficial to elucidate the mechanism underlying the anti-inflammatory and osteogenic effect of HSA-MDSPB NPs. Following injection into the periodontium, HSA-MDSPB NPs exert potent antioxidant and anti-inflammatory effects by scavenging exogenous oxidants and modulating signaling pathways. Finally, HSA-MDSPB NPs showed significant efficacy in inhibiting alveolar bone resorption through the reduction of inflammation and promotion of osteogenesis.

3. Conclusion

In conclusion, the development of HSA-MDSPB NPs as a potential nanomedicine for treatment for periodontitis has shown promising results due to its antioxidant, anti-inflammatory, and osteogenic functions. By virtue of multiple enzyme-like activities, HSA-MDSPB NPs with satisfactory biocompatibility could scavenge various ROS to relief oxidative stress both *in vitro* and *in vivo*. Meanwhile, HSA-MDSPB NPs have exhibited anti-inflammatory effects on cellular and periodontal tissues, as well as an immunoregulatory ability by promoting the polarization of BMDM towards an anti-inflammatory M2 type over a pro-inflammatory M1 type. Notably, HSA-MDSPB NPs promoted osteogenic differentiation of bone marrow stromal cells, resulting in less alveolar bone loss and enhanced periodontal tissue regeneration. Last but not least, our investigation into the underlying mechanism revealed the potential involvement of various pathways, including the HIF-1α and TLR-NF-κB pathway, in conferring anti-inflammatory function of HSA-

MDSPB NPs. Taken together, these versatile nanoparticles provide a novel platform for the therapy of periodontitis and a range of diseases featured with inflammation and bone resorption.

4. Experimental section

4.1. Synthesis of HSA-MDSPB NPs

In short, solutions containing 0.04 mM $K_4[Fe(CN)_6]$ (Sigma, USA) and 50 mg HSA (Sigma),as well as 0.05 mM $MnCl_2$ (Sigma) and 50 mg HSA, were prepared by dispersing and dissolved the respective components in 10 mL of distilled water. After stirring for 30 min, the two solutions were then mixed for another 1 h 24 h later at room temperature, the resulting solution was centrifuged at 13000 rpm for 15 min, and the precipitate was collected and further washed with distilled water three times. Ultimately, the powder of HSA-MDSPB NPs was acquired by lyophilization (Fig. S26A).

4.2. Characterization of HSA-MDSPB NPs

SEM and TEM images were taken from ZEISS Sigma 300 and JEOL JEM-2100F instruments respectively. Element mapping was performed using a field-emission Magellan 400 microscope. FTIR spectra were obtained from a Nicolet iS20 FTIR spectrometer (Thermo Fisher Scientific, USA). XPS analysis was conducted on a K-Alpha + X-ray photoelectron spectrometer (Thermo Fisher Scientific). Zeta potential and particle size distribution were measured in a phosphate buffer solution and in the same buffer solution after exposure to 10 % serum for 24 h using a Zetasizer Nanoseries instrument (Nano ZS90, UK).

4.3. ROS scavenging ability

The HSA-MDSPB NPs solution (1 mg/mL) contained in a dialysis bag was immersed in solutions of pH 7.4 and pH 6.5. After a 24 and 72 h later, the outer solution was collected for test of the Mn and Fe iron concentration using Inductively coupled plasma spectrometer (ThermoFisher, USA). The total antioxidant capacity of HSA-MDSPB NPs was detected by a total antioxidant capacity assay kit (mlbio, shanghai, China) according to manufacturer's instructions while POD enzyme activity was determined using TMB, a commonly utilized natural substrate for detecting POD activity, with absorbance readings at 650 nm recorded utilizing a microplate reader (BioTek Synergy HIM, USA). EPR spectra were obtained with a Bruker A300-10/12 spectrometer (Germany). HSA-MDSPB NPs were dissolved in a 20 % hydrogen peroxide solution, and bubbles indicative of oxygen production were observed.

4.4. Extraction and culture of MGFs, MM-BMSCs and BMDM

Gingiva or maxillary bone tissue from mice was collected, washed and cut into 1–2 mm^2 pieces. Subsequently, these tissue pieces were incubated in a 37 °C, 5 % CO_2 humidified incubator in DMEM (HyClone, USA) and αMEM (HyClone) with 10 % FBS (BI, Israel), 100 IU mL^{-1} penicillin G, and 100 ng mL^{-1} streptomycin antibiotic (HyClone). The culture medium was refreshed every two to three days. Upon reaching 80–90 % confluence, the cells were passaged using 0.25 % trypsin (HyClone) and replated at a 1:3 dilution ratio. The cells obtained from passage 3 were used in subsequent experiments.

Bone marrow mesenchymal cells were extracted from mouse bone marrow chambers. After a 2-day incubation period, the cells in the supernatant were collected and erythrocytes were lysed using a red blood cell lysis buffer (Solarbio, Beijing, China). Subsequently, the cells were resuspended in complete αMEM medium supplemented with M-CSF (30 ng mL^{-1}, Pepro Tech, USA). The culture medium was refreshed on the 3rd and 6th days. Bone marrow-derived macrophages (BMDM) were successfully differentiated and deemed suitable for further experimentation after 7 days.

4.5. CCK-8 assay

CCK-8 kits (Beyotime, Shanghai, China) were used to detect the viability of cells. Cells were initially plated at a density of 5.0×10^3 cells per well in a 96-well plate and allowed to adhere overnight. Subsequently, varying concentrations of HSA-MDSPB NPs (5, 10, 20, 40 and 80 µg mL^{-1}) were added to the wells, followed by a 24-h incubation period. The absorbance at 450 nm was measured using a microplate reader (BioTek Synergy HIM, USA) after treatment with CCK-8 solution for 4 h.

4.6. Uptake of HSA-MDSPB NPs

Following a 4-h period of cellular starvation, FITC-labeled HSA-MDSPB NPs were introduced to the cells, which were subsequently analyzed using fluorescence microscopy (Nikon, Japan) or flow cytometry (Beckman, USA) after a specified duration (2, 4 or 8 h). In a separate experimental condition, the cells were starved for 2 h and then treated with hypertonic sucrose (0.45 M), Methyl-β-cyclodextrin (3 mM) and Cytochalasin D (2 µM) in the corresponding group. After an additional 2-h incubation period, FITC-labeled HSA-MDSPB NPs were administered for 4 h, followed by incubation with Lyso-Tracker Red (Beyotime) as per the manufacturer's guidelines. The detection of cells was performed using fluorescence microscopy (Nikon, Japan) or flow cytometry (Beckman, USA).

4.7. Cell treatments

MGFs were exposed to *Escherichia coli* LPS (Sigma-Aldrich, USA) at a concentration of 100 ng mL^{-1}, either alone or in combination with HSA-MDSPB NPs at 20 µg mL^{-1} in complete DMEM medium for 8 h. MM-BMSCs were similarly treated with LPS at 10 ng mL^{-1}, with or without HSA-MDSPB NPs at 10 µg mL^{-1} in complete αMEM medium for 12 h. BMDM were stimulated with LPS at a concentration of 1 µg/mL in the presence or absence of HSA-MDSPB NPs at a concentration of 20 µg mL^{-1} in complete αMEM medium for a duration of 24 h.

4.8. Antioxidant property in vitro

The cell preparation protocol was consistent with the methodology outlined in the preceding section on cell treatment. Then the cells were cultured with DCFH-DA at a concentration of 10 µmol L^{-1} and incubated at 37 °C for a period of 20 min. Fluorescence images were captured by a microscope (ZEISS, Germany) and fluorescence intensity was detected by a flow cytometer (Beckman, USA).

4.9. Real-time quantitative polymerase chain reaction

Total RNA from cells or tissues was extracted from cells or tissues using the RNAiso Plus reagent (TaKaRa, Japan). The PrimeScript™ RT reagent kit with gDNA Eraser (Perfect Real Time) (TaKaRa) was employed for the reverse transcription of RNA into cDNA which was then utilized for qPCR analysis with SYBR Mix (Yeasen, Shanghai, China), specific primers (Table S1) and a LightCycler System (Roche, Switzerland). The gene expression levels were calculated and normalized using the $2^{-\Delta\Delta Ct}$ method relative to GAPDH.

4.10. Western blots

Cells lysis was achieved with RIPA buffer (Beyotime) supplemented with protease inhibitor, phosphatase inhibitor, EDTA, and PMSF. Following centrifugation at 12000 rpm for 10 min, the supernatant was collected for protein concentration determination. Then, 5× loading buffer (Sangon, Shanghai, China) was mixed with the protein solution and boiled at 100 °C for 5 min. Equal amounts of total protein from the lysates were separated by SDS-PAGE and transferred onto 0.22 µm

nitrocellulose membranes (Millipore, USA). Following incubation with a 5 % bovine serum albumin solution for 1 h, the membranes were exposed to primary antibodies overnight at 4 °C and subsequently to secondary antibodies for an additional hour. The blots were visualized using a chemiluminescence imaging system (Tanon 4600, Shanghai, China). The primary antibodies utilized were anti-β-actin, anti-IL-1β, anti-IL-6 (1:1000, Affinity, China), anti-TNF-α (1:500, Affinity), anti-MMP-9 (1:1000, Proteintech, Wuhan, China), anti-MMP-13 (1:500, Proteintech), anti-Arg1(1:1000, Santa Cruz, USA), anti-iNOS (1:1000, Santa Cruz), anti-RUNX2 (1:1000, bioss, Beijing, China), anti-OPN (1:2000, Proteintech), anti-TLR4 (1:2000, Santa Cruz), anti-P65, anti-P-P65 (1:1000, Affinity), and anti-HIF-1α (1:500, Santa Cruz).

4.11. ELISA analysis

Following various treatments of MGFs, the culture medium supernatant was collected for ELISA analysis of IL-6 and TNF-α concentrations using ELISA kits (Sangon) according to the manufacturer's instructions.

4.12. Alizarin red staining

After MM-BMSCs were isolated and cultured, they were seeded into 12-well plates at a density of 15×10^4 cells/mL. After 24 h, the MM-BMSCs were exposed to different culture conditions including complete αMEM (HyClone), complete αMEM + HSA-MDSPB NPs (10 µg/mL), osteogenic induction medium comprising 10 mM β-glycerophosphate (Sigma), 50 µg mL^{-1} ascorbic acid (Sigma), and 100 nM dexamethasone (Sigma), osteogenic induction medium + HSA-MDSPB NPs (10 µg/mL), complete αMEM + PB (10 µg/mL), and complete αMEM +Mn^{2+}-HSA (10 µg/mL). Following 14 and 21 days of culture, cells were subjected to staining with Alizarin red solution (OriCell, Guangzhou, China) as per the manufacturer's protocol. Subsequently, the cells were photographed at a magnification of 100× using light microscopy (Olympus, Japan).

4.13. Ligature-induced periodontitis mice model

C57BL/6 mice were housed in specific pathogen-free (SPF) cages in a random manner, with ad libitum access to standard food and water. Stringent measures were taken to ensure the provision of humane care to each animal and to minimize any potential suffering during the experimental procedures, in accordance with the National Institutes of Health Guidelines for the Care and Use of Laboratory Animals (NIH Publication No.85-23), last revised in 1996. All animal experiments conducted in this study were ethically approved by the Animal Welfare Committee of Stomatological Hospital of Tongji University (2020-DW-02). To establish a ligature-induced periodontitis mice model, the maxillary right second molars of 6-8-week-old male C57BL/6 mice were ligated with sterile 6-0 silk for either 7 or 14 days, with the contralateral side serving as a healthy control. Throughout the experimental period, mice receiving HSA-MDSPB NPs treatment were locally administered HSA-MDSPB NPs in saline (10 µL, 500 µg mL^{-1}) (Figs. S27A–C) via injection into the gums on the palatine side of the second molar once every two days until the time of sacrifice. Tissue samples from the maxillary bones, gingiva, spleen, heart, lungs, kidneys, and liver were collected for subsequent experiments.

4.14. Tissue distribution and ROS scavenging efficacy in vivo

HSA-MDSPB NPs loaded with IR783 were locally administered to mice, and luminescence images were captured by IVIS (Vieworks, Korea) at 4, 24, and 48-h intervals. C57BL/6 mice were randomly assigned to three groups and administered respective treatments. After 7 or 14 days, the mice were euthanized through anesthesia overdose. The ROS eliminating ability of HSA-MDSPB NPs was assessed by injecting the L012 reagent (MedChemExpress, USA) into each mouse via tail vein

before euthanasia. Luminescence images were detected by IVIS (Vieworks, Korea).

4.15. Tissue specimens, hematoxylin-eosin, masson and immunofluorescence staining

Tissues were fixed in 4 % paraformaldehyde (Macklin, Shanghai, China) at 4 °C for 48 h, decalcified in a 10 % ethylenediaminetetraacetic acid (Greagent, Shanghai, China) solution, dehydrated in an automatic dehydrator (Thermo Fisher Scientific), and embedded in paraffin wax (Leica, Germany) for sectioning into slices (approximately 4 μm thick). The sections underwent deparaffinization and hydration prior to staining with H&E (Beyotime) and Masson staining kit (Keygen biotech, China) following the manufacturer's instructions. For tissue immunofluorescence staining, antigen retrieval was performed by incubating the sections with hyaluronidase (Sigma) for 1 h at 37 °C, followed by blocking with 10 % goat serum (MXB, China). Then the sections were incubated overnight at 4 °C with primary antibodies targeting myeloperoxidase (1 μg μL^{-1}, R&D systems, USA), IL-1β (1:200, Affinity) and MMP-9 (1:500, Proteintech). After incubation with secondary antibodies for 1 h, the sections were stained with DAPI (Beyotime) for 5 min. High-resolution digital microscope (Nikon, Japan) was utilized to capture images.

4.16. Micro-computed tomography (Micro-CT) analysis

The maxillary bone was isolated from mice, fixed in 4 % paraformaldehyde for 48 h. Scanning was performed using a Scanco mCT 50 (Scanco Medical, Switzerland) at a resolution of 10 μm, with a voltage of 70 kV and an electric current of 200 mA. Then a 3D reconstruction image was generated, and measurements of the distance from the CEJ to the apex of the ABC were taken at various sites (mesial, middle and distal) on the maxillary second molar from both buccal and lingual perspectives. Representative X-ray images were also obtained in both sagittal and transverse planes. Moreover, a total of fifteen slices of the interalveolar septum between the first molar and second molar were reconstructed for statistical analysis, which included BMD and BV/TV.

4.17. In vivo biosafety evaluation

Male C57BL/6 mice aged 6–8 weeks were randomly assigned to one of the three groups: a control group, a group receiving HSA-MDSPB NPs in PBS at a dosage of 10 mg kg^{-1}, and a group receiving HSA-MDSPB NPs in PBS at a dosage of 20 mg kg^{-1}. The mice were sacrificed on the 28th day following intravenous administration of HSA-MDSPB NPs, and their spleen, heart, lungs, kidneys, and liver were collected for H&E staining. Blood samples were also collected for liver and kidney function tests, as well as routine blood tests.

4.18. RNA-seq and data analysis

Cellular RNA was extracted with the RNeasy mini kit (Qiagen, Germany) and assessed for quality and quantity using the Qubit 3.0 Fluorometer (Life Technologies, USA) and the Nanodrop One spectrophotometer (Thermo Fisher Scientific). The integrity of the total RNA was evaluated using the Agilent 2100 Bioanalyzer (Agilent Technologies, USA). Paired-end libraries were generated utilizing the mRNA-seq Lib Prep Kit for Illumina (ABclonal, China) according to the Sample Preparation Guide. Library construction and sequencing were proceeded by Sinotech Genomics Co., Ltd (Shanghai, China). The fragment abundance within each gene was calculated using Stringtie software and normalized by the TMM algorithm. Differential expression analysis was performed using the R package (version 3.4.3) (cutoff: |log2(FC)| value > 1, *p* value < 0.05 and one group's mean FPKM >1) while KEGG pathway analysis (Kyoto Encyclopedia of Genes and Genomes http://www.genome.ad.jp/kegg) and Gene Ontology (GO) functional

enrichment analysis were performed via the enrich R package (version 3.4.3).

4.19. Statistical analysis

The data are presented as the mean ± standard deviation (SD). Statistical analyses were performed using IBM SPSS 22.0 software, with comparisons of data exhibiting normal distribution and homogeneity of variance conducted through one-way ANOVA and the least significant difference (LSD) test for multiple post-hoc comparisons. A significance level of *p* < 0.05 (two-tailed) was employed.

CRediT authorship contribution statement

Bangping Cao: Writing – original draft, Visualization, Software, Methodology, Investigation, Formal analysis, Data curation, Conceptualization. **Xuanbo Da:** Writing – review & editing, Validation, Software, Methodology, Investigation, Data curation, Conceptualization. **Wenjing Wu:** Writing – review & editing, Methodology, Investigation. **Jian Xie:** Writing – review & editing, Investigation. **Xuejing Li:** Writing – review & editing, Methodology. **Xin Wang:** Writing – review & editing, Investigation. **Hui Xu:** Writing – review & editing, Investigation. **Jianfang Gao:** Writing – review & editing, Investigation. **Hui Yang:** Writing – review & editing, Methodology, Investigation. **Jiansheng Su:** Writing – review & editing, Supervision, Resources, Project administration, Funding acquisition, Conceptualization.

Declaration of competing interest

The authors declare that they have no known competing financial interests or personal relationships that could have appeared to influence the work reported in this paper.

Data availability

Data will be made available on request.

Acknowledgements

Appendix A. Supplementary data

Supplementary data to this article can be found online at https://doi.org/10.1016/j.mtbio.2024.101163.

References

[1] D. Trindade, R. Carvalho, V. Machado, L. Chambrone, J.J. Mendes, J. Botelho, Prevalence of periodontitis in dentate people between 2011 and 2020: a systematic review and meta-analysis of epidemiological studies, J. Clin. Periodontol. 50 (5) (May 2023) 604–626, https://doi.org/10.1111/jcpe.13769.

[2] H.A. Schenkein, P.N. Papapanou, R. Genco, M. Sanz, Mechanisms underlying the association between periodontitis and atherosclerotic disease, Periodontol. 2000 83 (1) (Jun 2020) 90–106, https://doi.org/10.1111/prd.12304.

[3] M. Sanz, A. Marco Del Castillo, S. Jepsen, et al., Periodontitis and cardiovascular diseases: consensus report, J. Clin. Periodontol. 47 (3) (Mar 2020) 268–288, https://doi.org/10.1111/jcpe.13189.

[4] A.I. Khumaedi, D. Purnamasari, I.P. Wijaya, Y. Soeroso, The relationship of diabetes, periodontitis and cardiovascular disease, Diabetes Metabol. Syndr. 13 (2) (Mar-Apr 2019) 1675–1678, https://doi.org/10.1016/j.dsx.2019.03.023.

[5] J. Gonzalez-Febles, M. Sanz, Periodontitis and rheumatoid arthritis: what have we learned about their connection and their treatment? Periodontol. 2000 87 (1) (Oct 2021) 181–203, https://doi.org/10.1111/prd.12385.

[6] M. Sadrameli, P. Bathini, L. Alberi, Linking mechanisms of periodontitis to Alzheimer's disease, Curr. Opin. Neurol. 33 (2) (Apr 2020) 230–238, https://doi.org/10.1097/WCO.0000000000000797.

[7] E.H. Kim, S. Nam, C.H. Park, et al., Periodontal disease and cancer risk: a nationwide population-based cohort study, Front. Oncol. 12 (2022) 901098, https://doi.org/10.3389/fonc.2022.901098.

[8] A. Guentsch, Antibiotics against periodontal biofilms, Monogr. Oral Sci. 29 (2021) 119–132, https://doi.org/10.1159/000510188.

[9] K. Jepsen, S. Jepsen, Antibiotics/antimicrobials: systemic and local administration in the therapy of mild to moderately advanced periodontitis, Periodontol. 2000 71 (1) (Jun 2016) 82–112, https://doi.org/10.1111/prd.12121.

[10] F. Graziani, D. Karapetsa, B. Alonso, D. Herrera, Nonsurgical and surgical treatment of periodontitis: how many options for one disease? Periodontol. 2000 75 (1) (Oct 2017) 152–188, https://doi.org/10.1111/prd.12201.

[11] H. Kanzaki, S. Wada, T. Narimiya, et al., Pathways that regulate ROS scavenging enzymes, and their role in defense against tissue destruction in periodontitis, Front. Physiol. 8 (2017) 351, https://doi.org/10.3389/fphys.2017.00351.

[12] Y.T. Chin, G.Y. Cheng, Y.J. Shih, et al., Therapeutic applications of resveratrol and its derivatives on periodontitis, Ann. N. Y. Acad. Sci. 1403 (1) (Sep 2017) 101–108, https://doi.org/10.1111/nyas.13433.

[13] Y. Weng, H. Wang, L. Li, Y. Feng, S. Xu, Z. Wang, Trem2 mediated Syk-dependent ROS amplification is essential for osteoclastogenesis in periodontitis microenvironment, Redox Biol. 40 (Apr 2021) 101849, https://doi.org/10.1016/j.redox.2020.101849.

[14] G. Huang, J. Zang, L. He, et al., Bioactive nanoenzyme reverses oxidative damage and endoplasmic reticulum stress in neurons under ischemic stroke, ACS Nano 16 (1) (Jan 25 2022) 431–452, https://doi.org/10.1021/acsnano.1c07205.

[15] H. Wei, E. Wang, Nanomaterials with enzyme-like characteristics (nanozymes): next-generation artificial enzymes, Chem. Soc. Rev. 42 (14) (Jul 21 2013) 6060–6093, https://doi.org/10.1039/c3cs35486e.

[16] J. Yang, J. Zhou, Y. Zhao, L. Zhu, G. Luo, B. Ge, Hollow CeO(2) with ROS-scavenging activity to alleviate colitis in mice, Int. J. Nanomed. 16 (2021) 6889–6904, https://doi.org/10.2147/IJN.S317261.

[17] D. Li, M. Liu, W. Li, et al., Synthesis of Prussian blue nanoparticles and their antibacterial, antiinflammation and antitumor applications, Pharmaceuticals 15 (7) (Jun 21 2022), https://doi.org/10.3390/ph15070769.

[18] M.A. Busquets, J. Estelrich, Prussian blue nanoparticles: synthesis, surface modification, and biomedical applications, Drug Discov. Today 25 (8) (Aug 2020) 1431–1443, https://doi.org/10.1016/j.drudis.2020.05.014.

[19] Z. Qin, Y. Li, N. Gu, Progress in applications of Prussian blue nanoparticles in biomedicine, Adv. Healthcare Mater. 7 (20) (Oct 2018) e1800347, https://doi.org/10.1002/adhm.201800347.

[20] W. Zhu, N.G.J. Richards, Biological functions controlled by manganese redox changes in mononuclear Mn-dependent enzymes, Essays Biochem. 61 (2) (May 9 2017) 259–270, https://doi.org/10.1042/EBC20160070.

[21] L. Pang, R. Zhao, J. Chen, et al., Osteogenic and anti-tumor Cu and Mn-doped borosilicate nanoparticles for syncretic bone repair and chemodynamic therapy in bone tumor treatment, Bioact. Mater. 12 (Jun 2022) 1–15, https://doi.org/10.1016/j.bioactmat.2021.10.030.

[22] F. Westhauser, S. Wilkesmann, Q. Nawaz, S.I. Schmitz, A. Moghaddam, A. R. Boccaccini, Osteogenic properties of manganese-doped mesoporous bioactive glass nanoparticles, J. Biomed. Mater. Res. 108 (9) (Sep 2020) 1806–1815, https://doi.org/10.1002/jbm.a.36945.

[23] B. Jia, H. Yang, Y. Han, et al., In vitro and in vivo studies of Zn-Mn biodegradable metals designed for orthopedic applications, Acta Biomater. 108 (May 2020) 358–372, https://doi.org/10.1016/j.actbio.2020.03.009.

[24] J. Zhang, Q. Zhang, S. Li, Y. Hou, H. Zhang, The effects of Mn(2+) on the proliferation, osteogenic differentiation and adipogenic differentiation of primary mouse bone marrow stromal cells, Biol. Trace Elem. Res. 151 (3) (Mar 2013) 415–423, https://doi.org/10.1007/s12011-012-9581-8.

[25] X. Mu, X. Yan, Q. Tian, J. Lin, S. Yang, BSA-assisted synthesis of ultrasmall gallic acid-Fe(III) coordination polymer nanoparticles for cancer theranostics, Int. J. Nanomed. 12 (2017) 7207–7223, https://doi.org/10.2147/IJN.S146064.

[26] T. Yang, Y. Wang, H. Ke, et al., Protein-nanoreactor-Assisted synthesis of semiconductor nanocrystals for efficient cancer theranostics, Adv. Mater. 28 (28) (Jul 2016) 5923–5930, https://doi.org/10.1002/adma.201506119.

[27] X. Man, S. Li, Q. Xu, et al., Developing a copper(II) isopropyl 2-pyridyl ketone thiosemicarbazone compound based on the IB subdomain of human serum albumin-indomethacin complex: inhibiting tumor growth by remodeling the tumor microenvironment, J. Med. Chem. 67 (7) (Apr 11 2024) 5744–5757, https://doi.org/10.1021/acs.jmedchem.3c02378.

[28] Z. Sheng, D. Hu, M. Zheng, et al., Smart human serum albumin-indocyanine green nanoparticles generated by programmed assembly for dual-modal imaging-guided cancer synergistic phototherapy, ACS Nano 8 (12) (Dec 23 2014) 12310–12322, https://doi.org/10.1021/nn5062386.

[29] Z. Zhang, J. Zhang, T. Yang, et al., Developing an anticancer platinum(II) compound based on the uniqueness of human serum albumin, J. Med. Chem. 66 (8) (Apr 27 2023) 5669–5684, https://doi.org/10.1021/acs.jmedchem.3c00001.

[30] Z. Liu, C. Li, Y. Cao, et al., Manganese(III) phthalocyanine complex nanoparticle-loaded glucose oxidase to enhance tumor inhibition through energy metabolism and macrophage polarization, ACS Appl. Bio Mater. 7 (3) (Mar 18 2024) 1862–1877, https://doi.org/10.1021/acsabm.3c01251.

[31] K. Xu, P. Huang, Y. Wu, et al., Engineered selenium/human serum albumin nanoparticles for efficient targeted treatment of Parkinson's disease via oral gavage, ACS Nano 17 (20) (Oct 24 2023) 19961–19980, https://doi.org/10.1021/acsnano.3c05011.

[32] J. Zhao, W. Gao, X. Cai, et al., Nanozyme-mediated catalytic nanotherapy for inflammatory bowel disease, Theranostics 9 (10) (2019) 2843–2855, https://doi.org/10.7150/thno.33727.

[33] C. Lennicke, H.M. Cocheme, Redox metabolism: ROS as specific molecular regulators of cell signaling and function, Mol. Cell 81 (18) (Sep 16 2021) 3691–3707, https://doi.org/10.1016/j.molcel.2021.08.018.

[34] C. Nathan, A. Cunningham-Bussel, Beyond oxidative stress: an immunologist's guide to reactive oxygen species, Nat. Rev. Immunol. 13 (5) (May 2013) 349–361, https://doi.org/10.1038/nri3423.

[35] F.S.C. Sczepanik, M.L. Grossi, M. Casati, et al., Periodontitis is an inflammatory disease of oxidative stress: we should treat it that way, Periodontol. 2000 84 (1) (Oct 2020) 45–68, https://doi.org/10.1111/prd.12342.

[36] Y. Yu, S. Zhao, D. Gu, et al., Cerium oxide nanozyme attenuates periodontal bone destruction by inhibiting the ROS-NFkappaB pathway, Nanoscale 14 (7) (Feb 17 2022) 2628–2637, https://doi.org/10.1039/d1nr06043k.

[37] G. Hajishengallis, Periodontitis: from microbial immune subversion to systemic inflammation, Nat. Rev. Immunol. 15 (1) (Jan 2015) 30–44, https://doi.org/10.1038/nri3785.

[38] W. Wang, C. Zheng, J. Yang, B. Li, Intersection between macrophages and periodontal pathogens in periodontitis, J. Leukoc. Biol. 110 (3) (Sep 2021) 577–583, https://doi.org/10.1002/JLB.4MR0421-756R.

[39] X. Sun, J. Gao, X. Meng, X. Lu, L. Zhang, R. Chen, Polarized macrophages in periodontitis: characteristics, function, and molecular signaling, Front. Immunol. 12 (2021) 763334, https://doi.org/10.3389/fimmu.2021.763334.

[40] L.C. Shanley, O.R. Mahon, D.J. Kelly, A. Dunne, Harnessing the innate and adaptive immune system for tissue repair and regeneration: considering more than macrophages, Acta Biomater. 133 (Oct 1 2021) 208–221, https://doi.org/10.1016/j.actbio.2021.02.023.

[41] C. Varol, A. Mildner, S. Jung, Macrophages: development and tissue specialization, Annu. Rev. Immunol. 33 (2015) 643–675, https://doi.org/10.1146/annurev-immunol-032414-112220.

[42] C.D. Mills, K. Kincaid, J.M. Alt, M.J. Heilman, A.M. Hill, M-1/M-2 macrophages and the Th1/Th2 paradigm, J. Immunol. 164 (12) (Jun 15 2000) 6166–6173, https://doi.org/10.4049/jimmunol.164.12.6166.

[43] S. Wang, R. Liu, Q. Yu, L. Dong, Y. Bi, G. Liu, Metabolic reprogramming of macrophages during infections and cancer, Cancer Lett. 452 (Jun 28 2019) 14–22, https://doi.org/10.1016/j.canlet.2019.03.015.

[44] R.J.W. Arts, M.G. Netea, Adaptive characteristics of innate immune responses in macrophages, Microbiol. Spectr. 4 (4) (Aug 2016), https://doi.org/10.1128/microbiolspec.MCHD-0023-2015.

[45] A. Bernar, J.V. Gebetsberger, M. Bauer, W. Streif, M. Schirmer, Optimization of the alizarin red S assay by enhancing mineralization of osteoblasts, Int. J. Mol. Sci. 24 (1) (Dec 31 2022), https://doi.org/10.3390/ijms24010723.

[46] C. Wang, S. Stockl, S. Li, et al., Effects of extracellular vesicles from osteogenic differentiated human BMSCs on osteogenic and adipogenic differentiation capacity of naive human BMSCs, Cells 11 (16) (Aug 11 2022), https://doi.org/10.3390/cells11162491.

[47] D. Murugan Girija, Y.R.R. S, M. Kalachaveedu, R. Subbarayan, Osteogenic differentiation of human gingival mesenchymal stem cells by Aristolochia bracteolata supplementation through enhanced Runx2 expression, J. Cell. Physiol. 232 (7) (Jul 2017) 1591–1595, https://doi.org/10.1002/jcp.25835.

[48] S. El-Habashy, H. Eltaher, A. Gaballah, R. Mehanna, A.H. El-Kamel, Biomaterial-Based nanocomposite for osteogenic repurposing of doxycycline, Int. J. Nanomed. 16 (2021) 1103–1126, https://doi.org/10.2147/IJN.S298297.

[49] M. Rezai Rad, D. Liu, H. He, et al., The role of dentin matrix protein 1 (DMP1) in regulation of osteogenic differentiation of rat dental follicle stem cells (DFSCs), Arch. Oral Biol. 60 (4) (Apr 2015) 546–556, https://doi.org/10.1016/j.archoralbio.2014.12.013.

[50] X. Li, H. Wang, X. Yu, et al., Maladaptive innate immune training of myelopoiesis links inflammatory comorbidities, Cell 185 (10) (2022) 1709–1727.e18, https://doi.org/10.1016/j.cell.2022.03.043.

[51] M. Tang, G. Wang, J. Li, et al., Flavonoid extract from propolis alleviates periodontitis by boosting periodontium regeneration and inflammation resolution via regulating TLR4/MyD88/NF-κB and RANK/NF-κB pathway, J. Ethnopharmacol. 319 (2024) 117324, https://doi.org/10.1016/j.jep.2023.117324.

[52] S. Bose, G. Fielding, S. Tarafder, A. Bandyopadhyay, Understanding of dopant-induced osteogenesis and angiogenesis in calcium phosphate ceramics, Trends Biotechnol. 31 (10) (Oct 2013) 594–605, https://doi.org/10.1016/j.tibtech.2013.06.005.

[53] J. Hreha, A. Wey, C. Cunningham, et al., Local manganese chloride treatment accelerates fracture healing in a rat model, J. Orthop. Res. 33 (1) (Jan 2015) 122–130, https://doi.org/10.1002/jor.22733.

[54] J. Zhang, D. Tong, H. Song, et al., Osteoimmunity-Regulating biomimetically hierarchical scaffold for augmented bone regeneration, Adv. Mater. 34 (36) (Sep 2022) e2202044, https://doi.org/10.1002/adma.202202044.

[55] Z. Xu, Y. Liu, R. Ma, et al., Thermosensitive hydrogel incorporating Prussian blue nanoparticles promotes diabetic wound healing via ROS scavenging and mitochondrial function restoration, ACS Appl. Mater. Interfaces 14 (12) (Mar 30 2022) 14059–14071, https://doi.org/10.1021/acsami.1c24569.

[56] D.X. Tang, K. Liu, J.Y. Yang, et al., Artificial nonenzymatic antioxidant Prussian blue/KGM-BSA nanocomposite hydrogel dressing as ROS scavenging for diabetic wound healing, Int. J. Biol. Macromol. 266 (Pt 1) (May 2024) 131106, https://doi.org/10.1016/j.ijbiomac.2024.131106.

[57] W. Li, Y. Bei, X. Pan, et al., Selenide-linked polydopamine-reinforced hybrid hydrogels with on-demand degradation and light-triggered nanozyme release for diabetic wound healing, Biomater. Res. 27 (1) (May 18 2023) 49, https://doi.org/10.1186/s40824-023-00367-w.

[58] Z. Liu, Z. Luo, H. Yu, et al., Near-infrared light-controlled kartogenin delivery of multifunctional Prussian blue nanocomposites for cartilage defect repair, Nanoscale 15 (20) (May 25 2023) 9076–9093, https://doi.org/10.1039/d3nr00205e.

[59] B. Jia, H. Yang, Z. Zhang, et al., Biodegradable Zn-Sr alloy for bone regeneration in rat femoral condyle defect model: *in vitro* and *in vivo* studies, Bioact. Mater. 6 (6) (Jun 2021) 1588–1604, https://doi.org/10.1016/j.bioactmat.2020.11.007.

[60] Y. Gou, Y. Huang, W. Luo, et al., Adipose-derived mesenchymal stem cells (MSCs) are a superior cell source for bone tissue engineering, Bioact. Mater. 34 (Apr 2024) 51–63, https://doi.org/10.1016/j.bioactmat.2023.12.003.

[61] Z. Li, Y. Li, C. Liu, Y. Gu, G. Han, Research progress of the mechanisms and applications of ginsenosides in promoting bone formation, Phytomedicine 129 (Jul 2024) 155604, https://doi.org/10.1016/j.phymed.2024.155604.

[62] J.W. Lowery, V. Rosen, The BMP pathway and its inhibitors in the skeleton, Physiol. Rev. 98 (4) (Oct 1 2018) 2431–2452, https://doi.org/10.1152/physrev.00028.2017.